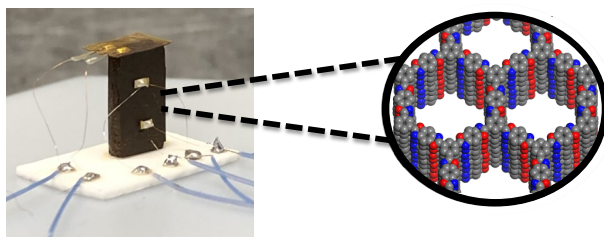


Thermal Conductivity of Two-Dimensional Benzobisoxazole-Linked Covalent Organic Frameworks with Nanopores: Implications for Thermal Management Applications

Erica M. Moscarello,^a Brandi L. Wooten,^b Hasnain Sajid,^e Logan D. Tichenor,^a Joseph P. Heremans,^{b,c,d} Matthew A. Addicoat,^e Psaras L. McGrier^{a*}

^aDepartment of Chemistry and Biochemistry, The Ohio State University, Columbus, Ohio 43210, United States; ^bDepartment of Materials Science and Engineering, Columbus, Ohio 43210, United States; ^cDepartment of Mechanical and Aerospace Engineering, The Ohio State University, Columbus, Ohio 43210, United States; ^dDepartment of Physics, The Ohio State University, Columbus, Ohio 43210, United States; ^eSchool of Science & Technology, Nottingham Trent University, Nottingham, NG11 8NS, UK

Supporting Information Placeholder



ABSTRACT: Thermal management is essential for maintaining the optimal performance of electronic devices. Although covalent organic frameworks have emerged as a platform for gas and energy storage applications, their thermal transport properties are greatly understudied. Herein, we report the thermal conductivities of three benzobisoxazole-linked (BBO) COFs with nanopores ranging from 1.3 to 2.5 nm over a wide temperature range (80 – 300 K) using the longitudinal, steady-state heat flow method. In doing so, thermal conductivity values as high as $0.677 \text{ W m}^{-1} \text{ K}^{-1}$ at 300 K were obtained, and no relationship between thermal conductivity and pore size was observed. These results were supported by DFT calculations. The thermal conductivities of the BBO-COFs doped with poly-3-hexylthiophene were also investigated. The BBO-COFs could be useful as ultra-low- k materials for thermal management applications.

1. INTRODUCTION

Covalent organic frameworks (COFs)¹⁻⁴ are an advanced class of crystalline porous polymers that contain high surface areas, tunable pore sizes, and high thermal stabilities. The modular nature of COFs allows their carbon skeletons to be tailored for a wide range of applications including catalysis,^{5, 6} sensing,⁷⁻⁹ energy storage,¹⁰⁻¹² gas storage,^{13, 14} and drug delivery.^{15,16} Although many COF-based systems have been investigated for a plethora of applications, their thermal management properties are greatly understudied.

Thermal management is crucial for ensuring the optimal performance and longevity of electronic devices and spacecraft.^{17,18} COFs offer the unique opportunity to embed various covalent linkages and π -conjugated units along the pore wall to enforce long-range π - π stacking interactions and tune the thermal transport properties of the polymeric system. Esteves and co-workers have shown the bulk

powders of four imine-linked three-dimensional (3D) COFs exhibit thermal conductivities (k) ranging from 0.038 to $0.048 \text{ W m}^{-1} \text{ K}^{-1}$.¹⁹ The thermal conductivities increased with decreasing pore size, a trend that has also been observed by Wilmer and coworkers via molecular dynamics simulations in some metal organic frameworks (MOFs).²⁰ Interestingly, Dichtel, Hopkins, and co-workers have shown that two-dimensional (2D) boronate-ester linked COF thin-films containing various π -conjugated monomer units exhibit thermal conductivities as high as $1 \text{ W m}^{-1} \text{ K}^{-1}$ in the cross-plane direction making them potentially useful for low- k dielectric applications.²¹ While this particular result demonstrates the promise of using COF-based systems for thermal management processes, more fundamental research examining different covalent linkages and π -conjugated monomers is greatly needed to further probe their thermal transport properties.

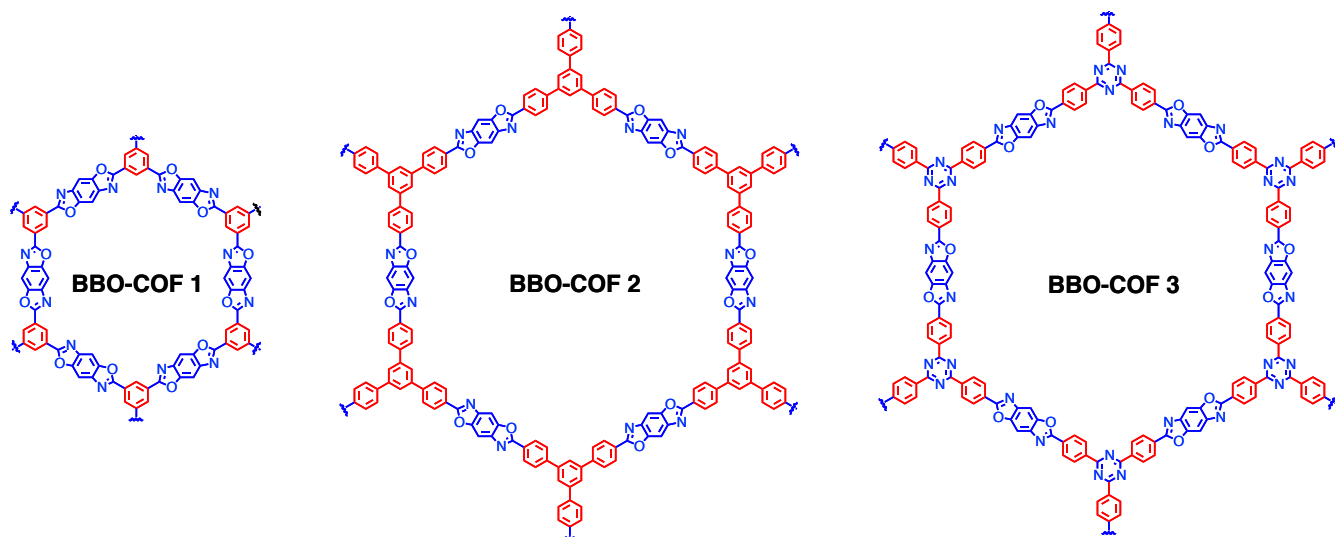


Figure 1. Structures of BBO-COFs 1, 2, and 3

Wang, Cahill, and co-workers have shown²² that liquid crystalline fibers of one-dimensional (1D) polybenzobisoxazole (PBO) polymers exhibit thermal conductivities of $\sim 20 \text{ W m}^{-1} \text{ K}^{-1}$ at room temperature. The high value is driven by longitudinal acoustic phonons that propagate along the PBO chain. Although this result indicates the 1D PBO display interesting thermal transport capabilities, the thermal conductivity of 2D COFs containing benzobisoxazole (BBO)^{23,24} linkages have not been examined. Thus, we were curious to see if the ordered nature of the polycrystalline 2D BBO-COF layers would provide thermal conductivity values similar to or higher than the 1D PBO system.

Herein, we report the thermal conductivities of three BBO-COF pellets containing 1,3,5-triformylbenzene (TFB), 1,3,5-tris(4-formylphenyl)benzene (TFPB), and 1,3,5-tris(4-formylphenyl)triazine (TFPT) units (Figure 1). The thermal conductivities of the pellets were measured over a wide temperature range (80 K – 300 K) using the longitudinal, steady-state heat flow method yielding values ranging from 0.391 to 0.677 $\text{W m}^{-1} \text{ K}^{-1}$ at 300 K. Surprisingly, the increase in thermal conductivity of the BBO-COFs was directly proportional to the increase in temperature, and was not dependent on the pore size of materials. Computational modelling of the thermal conductivity at 80 and 300 K supports the lack of pore size dependence, with very similar thermal conductivities for BBO-COF-1 and -2, and a moderate increase in conductivity for BBO-COF-3. In addition, we also investigated filling the BBO-COF pores with poly-3-hexylthiophene (p3HT),²⁵ a 1D polymer with thermal conductivity values of $\sim 2.2 \text{ W m}^{-1} \text{ K}^{-1}$, to further enhance their thermal transport properties. This is the first time, presumably, that the thermal conductivities of 2D BBO-COFs with nanopores have been investigated. The BBO-COFs could be useful as ultra-low- k materials for thermal management applications.

2. EXPERIMENTAL SECTION

2.1 Materials. Unless stated otherwise, all reagents were purchased from commercial sources and used without further purification.

2.2 Preparation of monomers, polymers, & BBO-COFs. All monomers, polymers, and BBO-COFs were synthesized according to previously reported literature procedures.^{23,24,42} Each p3HT-COF composite was prepared by stirring the COF with 0.05 equivalents of p3HT in dichloromethane (DCM) for 24 hours under nitrogen atmosphere. The solids were then filtered, washing with DCM until the solvent ran clear (ca. 150 mL).

2.3 Materials Characterization. Infrared spectra were recorded on a Thermo Scientific Nicolet iS5 with an iD7 diamond ATR attachment and are uncorrected. UV-vis diffuse reflectance spectra were gathered on an Agilent Technologies Cary Series UV-Vis-NIR Spectrophotometer. Surface area measurements, ¹H NMR and ¹³C cross-polarization magic angle spinning (CP-MAS) spectra were performed using established procedures.¹⁰

The powder X-ray diffraction studies were carried out on a Bruker Kappa Photon II CPAS diffractometer equipped with Cu K α radiation ($\lambda = 1.54178$). Data was collected at ambient conditions using a 360° phi-scan on a sample that was mounted on a Cryoloop using minimal Trilene Q-1100 oil. Sample-to-detector distance was 190 mm with an exposure time of 300 s per scan. Diffraction images were merged/integrated in DIFFRAC.EVA to produce 2D plots.

2.4 Preparation of samples for thermal conductivity measurements. Materials were pressed into pellets with a model C Carver laboratory press. Powders were grinded with a mortar and pestle before pressing under ca. 8 metric tons of pressure for ca. 5-10 minutes. The materials were pressed into disc-shaped pellets with diameters of 13 mm. Thicknesses of the pellets ranged from approximately 1-2.4 mm. A razor blade was used to cut the pellet into rectangular prisms for the analysis. The cut rectangular pellets ranged in width from approximately 3-6 mm and were under 8 mm in height. The thicknesses and widths of the pellets were measured using calipers. The widths were measured at three different points and averaged to accommodate for any variations.

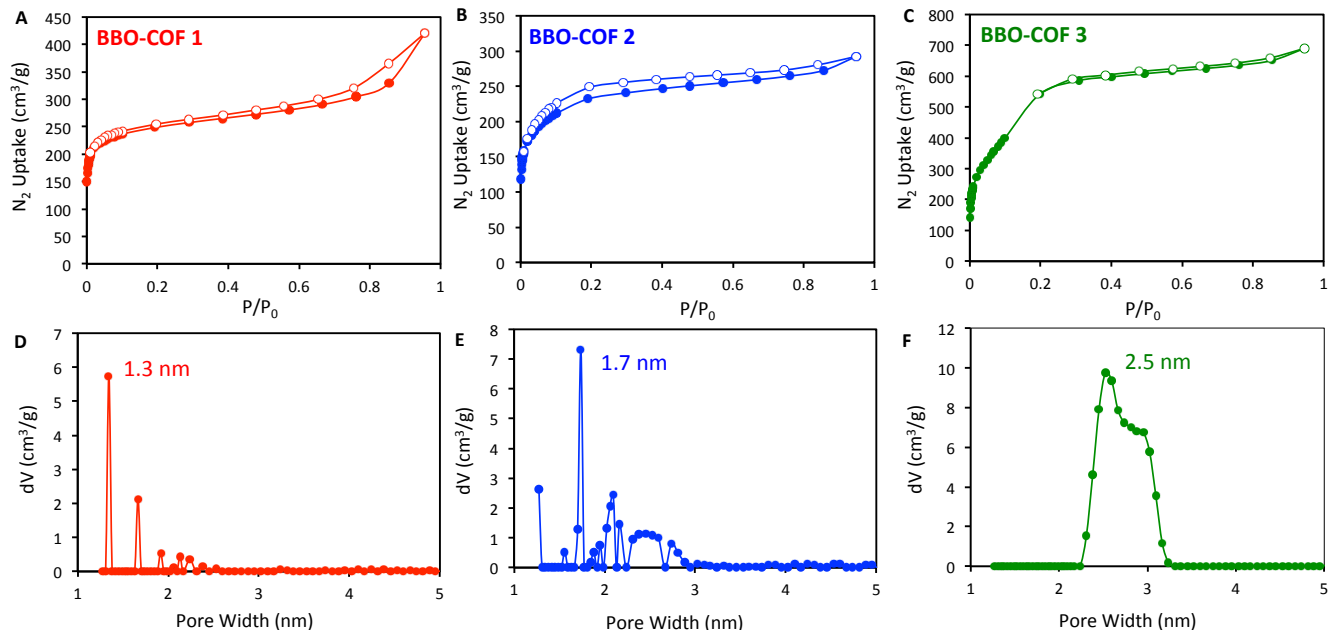


Figure 2. N₂ gas adsorption/desorption isotherms (A-C) and NLDFT pore size distributions (D-F) for BBO-COFs 1 (red), 2 (blue) and 3 (green).

The thermal conductivity of the polymers was evaluated using the longitudinal, steady-state heat flow method. Each of the pellet samples was prepared as follows. Two thermocouples were prepared using a copper and constantan wire (Omega Engineering, Norwalk CT, USA). Conductive silver epoxy (EpoTek, Bellerica, MA, USA) was used to secure the wires onto a small brass plate. A minimal amount of GE varnish was used to attach each brass plate

to the pellet. The distances between the hot and cold thermocouples ranged from approximately 1-3 mm. The distances were measured with calipers under a microscope. A resistive heater (Omega Engineering, Norwalk, CT, USA) was attached atop the pellet with minimal GE varnish. Two copper wires were used for current input to the heater. Alumina plates (MTI Corporation, Richmond, CA, USA) acted as heat sinks. Six small brass plates were attached to the base using epoxy. Perfluoroalkoxy (PFA) coated copper wires with a diameter of 0.003 cm were each soldered onto a brass plate. The pellet was mounted to the alumina base with a minimal amount of GE varnish. Wires from the thermocouples and heaters were each soldered to a brass plate (Figure 3a). The GE varnish was allowed to cure for 24 hours prior to performing measurements.

The sample was glued onto the copper cryostat arm (Figure S2). Each PFA-coated copper wire was soldered onto a cryostat pin. A heat shield was used to minimize radiation loss. All the wires connected to the sample were 25 μ m in diameter and the instrument was placed under a thermal vacuum to minimize conductive losses. The correction for the thermal conductance of the heat losses, K_{Loss} , was determined by measuring a sample of electrolytic iron, a National Bureau of Standards standard for thermal conductivity.

Four sample pellets were prepared for each material. The measured thermal conductivities were averaged at each temperature point.

2.5 Thermal conductivity measurements. Thermal conductivity measurements were determined using the longitudinal, steady-state heat flow method on a Janis cryostat system (Lake Shore Cryotronics, Westerville, OH, USA). The thermal conductivity was measured orthogonal to the direction the pellet was pressed. The cryostat was evacuated prior to cooling with liquid nitrogen to 79 K. Measurements were taken incrementally at every 20 K up to 300 K.

At each temperature point a current was applied to the heater. 40 minutes were given to allow for steady and stable readings before the voltage outputs of each thermocouple was collected. These voltage outputs were converted into temperature readings, T_H and T_C for the hot and cold thermocouples, respectively.

$$T_H = \frac{V_H - V_{Hres}}{a(T) * 10^{-6}}$$

$$T_C = \frac{V_C - V_{Cres}}{a(T) * 10^{-6}}$$

Where $a(T)$ is the effective Seebeck coefficient and $V_{H/C}$ and $V_{H/Cres}$ are the voltage and residual voltage outputs of the hot and cold thermocouples. The temperature difference (ΔT) was calculated by

$$\Delta T = T_H - T_C$$

The power (Pow) of the heater was calculated by

$$Pow = I * V$$

where I is the applied current and V is the voltage of the heater. The thermal conductivity was calculated by where

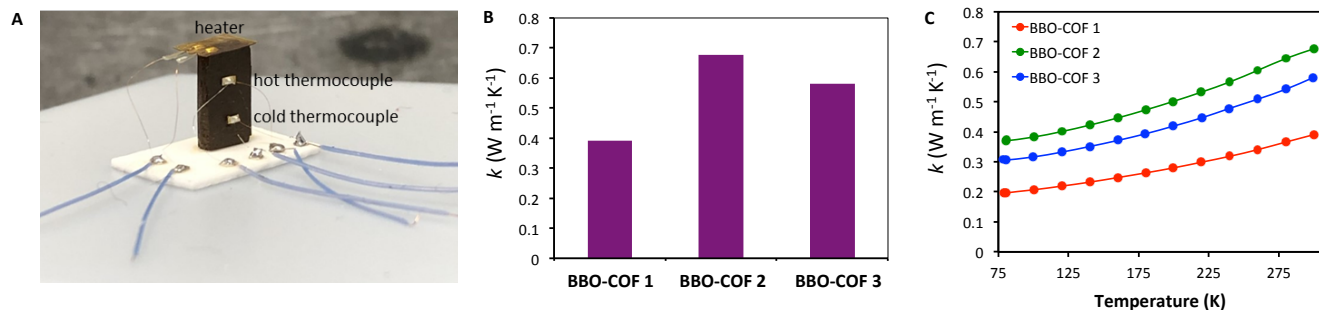


Figure 3. (A) Picture of the mounted BBO-COF pellet experimental set-up. (B) Thermal conductivity of the BBO-COFs at 300 K. (C) Temperature-dependent thermal conductivity profiles for the BBO-COFs. Estimated geometry uncertainty is about 9%.

$$\kappa = \left(\frac{Pow}{\Delta T} - K_{Loss} \right) * \frac{l}{w * t}$$

w is the width of the pellet, t , the thickness, and l , the distance between the hot and cold thermocouples.

2.5 Computational calculations. The temperature-dependent thermal conductivity of BBO-COF(s) was determined by using the non-equilibrium molecular

dynamics (NEMD)^{26,27} approach, as implemented in Amsterdam Modelling Suite (AMS) version 2021.1 by Software for Chemistry and Materials (SCM).²⁸ NEMD is a direct method of calculating the thermal conductivity of a periodic material in which the simulation cell is divided into heat source and sink regions to impose a steady heat flux through the finite conduction region. The thermal conductivity (k) of a material in the direction of interest can be determined according to Fourier’s law;^{29,30}

$$Q = k \frac{\Delta T}{L}$$

Where ΔT is the temperature gradient along the length of the conduction zone (L) between the hot and cold region while Q is the heat flux that can be calculated from the energy transfer rate between source and sink regions using the equation below

$$Q = \frac{\left(\frac{dE/dt}{2} \right)}{S}$$

where S is the cross-sectional area and the division by 2 is used because of periodic boundary conditions such as the heat transfers in two directions.

Prior to the thermal conductivity calculations, the BBO-COF(s) were first optimized at GFN1-xTB³¹ with fully relaxed lattice parameters and atomic positions using the density functional theory tight-binding (DFTB) engine. In the subsequent step, thermal conductivity calculations

were set up using NEMD simulations using the Universal Force Field.³²

In NEMD simulations, the BBO-COF systems were initially equilibrated at the targeted temperatures of 80 K and 300 K using the global Berendsen thermostat for 3×10^5 steps. Subsequently, a global thermostat was switched to the two local Nosé-Hoover³³⁻³⁵ thermostats to realize the hot and cold thermal baths. The NVT simulations with local thermostats (80 ± 10 & 300 ± 10) were run for 1×10^6 steps. The time steps for all the thermal conductivity simulations were 1 fs.

Unlike the equilibrium molecular dynamics (EMD) method, the NEMD method exhibits a much more severe finite-size effect because it requires a separate heat source and a sink thermostat.³⁶ The finite-size effects occur when the length of the simulation unit cell is not significantly larger than the phonon mean free path.³⁷ In a small simulation unit cell, there may not be enough phonon modes to establish transport and scattering through the conduction region.³⁸ The effects of the size of unit cells on the thermal conductivity of BBO-COF(s) have also been investigated. To investigate the simulation-size effects on the BBO-COF(s) at 80 K and 300 K, the unit cells ranged from one to four in a and b directions.

3. RESULTS/DISCUSSION

3.1. Porosity of BBO-COFs. BBO-COF 1 and 2 exhibited type I isotherms revealing BET surface areas of 920 and 992 m² g⁻¹, while BBO-COF 3 exhibited a type IV isotherm with a BET surface area of 1684 m² g⁻¹ (Figure 2). Estimation of the NLDFT pore size distributions yielded average pore sizes of 1.3, 1.7 and 2.5 nm for BBO-COFs 1, 2, and 3, respectively. The experimental pore size of the BBO-COFs 1, 2 and 3 are lower than the theoretical pore sizes of 1.8, 3.3, and 3.3 nm, respectively. This data suggests that the layers of BBO-COFs 1, 2 and 3 are offset by ~ 0.5 , 1.6, and 0.8 nm, respectively, which is similar to what has been reported.^{23,24} In addition, the powder x-ray diffraction (PXRD) profiles are also consistent with their previously reported patterns (Figure S16-S21).

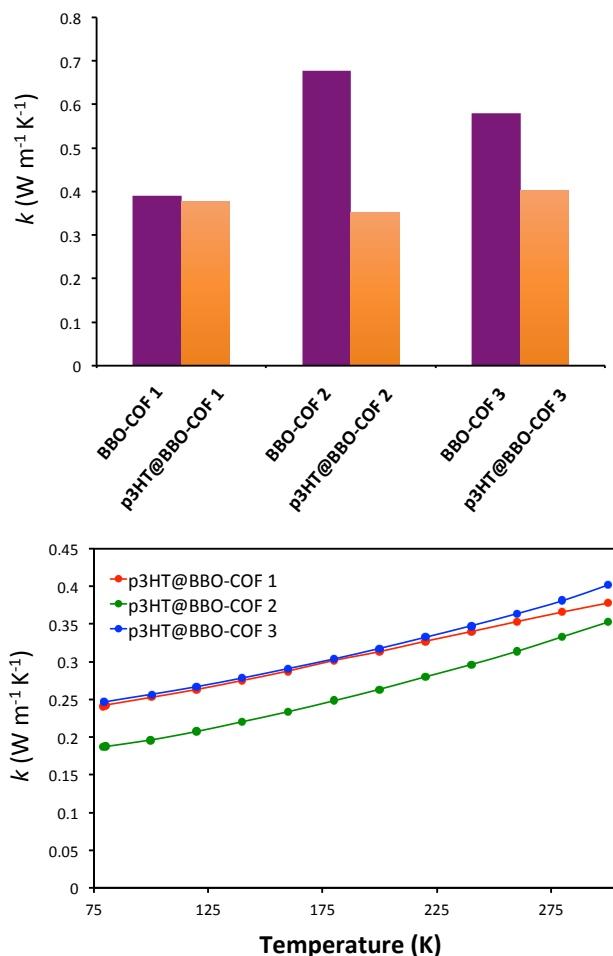


Figure 4. (Top) Thermal conductivity comparison between the BBO-COFs and p3HT@BBO-COF composites at 300 K. (Bottom) Temperature-dependent thermal conductivity profiles for the p3HT@BBO-COF composites. Estimated geometry uncertainty is about 9%.

3.2 Thermal conductivity of BBO-COFs. The thermal conductivity of each BBO-COF pellet was obtained by taking the average of four samples at each temperature point (Figure 3, Tables S7-S14). Surprisingly, BBO-COF 1 exhibited the lowest thermal conductivities ranging from 0.196 to 0.391 $\text{W m}^{-1} \text{K}^{-1}$ over a temperature range of 80-300 K. In contrast, BBO-COF 2 and BBO-COF 3 exhibited similar thermal conductivities of 0.375 to 0.677 $\text{W m}^{-1} \text{K}^{-1}$, and 0.308 to 0.581 $\text{W m}^{-1} \text{K}^{-1}$, respectively, from 80-300 K. Interestingly, the thermal conductivity of the BBO-COFs was directly proportional to the increase in temperature. The thermal conductivities of crystalline materials tends to decrease with temperature due to anharmonic phonon-phonon scattering processes,³⁹ and previous studies have shown^{19,20} that the thermal conductivity of porous materials often decreases with increasing pore size. However, it is unclear at the moment why the 2D BBO-COFs do not seem to follow either trend, but it could be related to the slip-stacked nature of the adjacent layers.^{23,24} **In contrast to BBO-COF 1, we believe that the higher thermal conductivity values for BBO-COF 2 and 3 are due to an increase in the aromatic units along the pore walls of the COFs. This feature could enhance the π - π interactions between the adjacent layers improving phonon transport.²⁵ In addition, the**

computed thermal conductivities support the role of planarity in increasing conductivity, with BBO-COF 3, which structurally differs from BBO-COF 2 by replacing the central benzene with triazine (Figure S54, Table S26). Replacing CH with N decreases the steric hinderance experienced by the three

phenyl groups, resulting in a (more) planar geometry. Consequently, calculated BBO-COF 3 conductivities are *ca.* 150% of those calculated for BBO-COF 1 and 2.

Due to the unexpected discrepancies in the results, the structural integrity of the BBO-COF pellets were further examined. XRD analysis revealed that the BBO-COF pellets retained their crystallinity (Figures S16, S18, & S20), but the BET surface areas drastically decreased from the pristine powders (Tables S1-S3). Interestingly, the pore sizes of BBO-COF 1 and BBO-COF 2 increased slightly by ~ 0.1 nm, and the pore size of BBO-COF 3 decreased by ~ 0.2 nm. However, no significant relationships could be discerned between the PXRDs, pore sizes and surface areas of the COFs to explain the differences in thermal conductivity values.

3.3 Characterization and Thermal Conductivity p3HT@BBO-COF Composite Materials. There is some evidence that filler materials can be used to improve the thermal conductivity of COFs. For instance, dynamic simulations from Feng, Feng and co-workers have shown⁴⁰ that doping COF-1 with C_{60} could increase the thermal conductivity from 1 to 10 $\text{W m}^{-1} \text{K}^{-1}$. Inspired by this result, we were curious to see if threading p3HT polymers through the BBO-COFs would produce similar results. Thin-films of p3HT have exhibited thermal conductivities up to 2.2 $\text{W m}^{-1} \text{K}^{-1}$ making them potentially useful for forming composite materials with enhanced thermal transport properties.²⁵

The p3HT@BBO-COFs were characterized using FT-IR, ¹³C CP-MAS, and UV-vis diffuse reflectance spectroscopy. FT-IR spectra showed the appearance of peaks at 2853, 2922, and 2953 cm^{-1} in all three composites, which is indicative of the sp^2 C-H stretching vibrations from the hexyl substituent on p3HT unit (Figures S22-S24). In comparison to the ¹³C CP-MAS of the BBO-COFs, new peaks emerged at 10.8, 19.5, 26.5, 28.8, 126, 129, and 132 ppm (Figures S25-S27) also corresponding to the p3HT unit. UV-vis diffuse reflectance spectra of the BBO-COFs shows that the materials absorb within the 350-450 nm range. Upon the incorporation of the p3HT into the pores of the BBO-COF systems, the adsorption band extends from 350 nm to ~ 650 nm, which overlaps well with the absorption band of p3HT (Figures S28-S30). In addition, PXRD analysis revealed that the composite materials do retain their crystallinity (Figure S17, S19, and S21). Nitrogen adsorption isotherms of the composite materials showed a dramatic reduction in surface areas from 920 to 264, 992 to 414, and 1684 to 709 m^2/g for p3HT@BBO-COF 1, p3HT@BBO-COF 2, and p3HT@BBO-COF 3, respectively (Tables S1-S3). The collected data indicates the successful incorporation of p3HT into the pores of the BBO-COFs.

The thermal conductivity of each p3HT@BBO-COF composite was obtained by taking the average of four samples at each temperature point (Figure 4, Tables S18-S25). Interestingly, p3HT@BBO-COF 2 exhibited the lowest thermal conductivities ranging from 0.186 to 0.353 $\text{W m}^{-1} \text{K}^{-1}$ over a temperature range of 80-300 K. In comparison, the

p3HT composites of BBO-COFs 1 and 3 exhibited similar thermal conductivities of 0.242 to 0.378 W m⁻¹ K⁻¹, and 0.246 to 0.402 W m⁻¹ K⁻¹, respectively, from 80-300 K. Although these values were higher than the thermal conductivity of p3HT (0.288 W m⁻¹ K⁻¹ at 300 K, see Figure S39), the thermal conductivities of the p3HT@BBO-COF composites were slightly lower than BBO-COFs 2 & 3. In comparison to the BBO-COFs, we expected the thermal conductivities of the p3HT@BBO-COF composites to increase due to the addition of possible heat transfer pathways, but this trend was not observed. It is possible that p3HT exists as a disordered matrix inside the pores of the BBO-COFs with no ability to form favorable π - π stacking interactions with the other p3HT units. The presence of the p3HT units could also disrupt some of the π - π stacking between the BBO-COF layers. These features could be responsible for lowering the thermal conductivity of the p3HT@BBO-COF composites.

4. CONCLUSION

In summary, we have examined the thermal transport properties of 2D BBO-COFs and p3HT@BBO-COF composites with nanopores ranging from 1.3 to 2.5 nm. While the BBO-COFs exhibited thermal conductivities as high as 0.677 W m⁻¹ K⁻¹ at 300 K, filling the pores of the materials with p3HT did not improve their thermal transport properties. There was no strong correlation between the pore size and thermal conductivity, but the increase in thermal conductivity was directly proportional to the increase in temperature for all of the materials. We believe that BBO-COFs could be useful as ultra-low-*k* materials for thermal management applications. Since the pores of the BBO-COFs can accommodate a variety of guests (C₆₀, gases, etc.), it is possible that the thermal-transfer performance of the materials could be improved under the right experimental conditions.^{40,41}

ASSOCIATED CONTENT

Supporting Information

The Supporting Information is available free of charge on the ACS Publications website.

Experimental details, BBO-COF characterization, nitrogen isotherms, and DFT calculations. (PDF)

AUTHOR INFORMATION

Corresponding Author

Psaras L. McGrier – *Department of Chemistry and Biochemistry, The Ohio State University, Ohio 43210, United States*; orcid.org/0000-0001-7637-4349; Email: mcgrier.1@osu.edu

Authors

Erica M. Moscarello – *Department of Chemistry and Biochemistry, The Ohio State University, Columbus, Ohio 43210, United States*

Brandi L. Wooten – *Department of Materials Science and Engineering, The Ohio State University, Columbus, Ohio 43210, United States*

Hasnain Sajid – *School of Science & Technology, Nottingham Trent University, Nottingham, NG11, 8NS, United Kingdom*

Logan D. Tichenor – *Department of Chemistry and Biochemistry, The Ohio State University, Ohio 43210, United States*

Matthew A. Addicoat – *School of Science & Technology, Nottingham Trent University, Nottingham, NG11, 8NS, United Kingdom*

Joseph P. Heremans – *Department of Materials Science and Engineering, The Ohio State University, Columbus, Ohio 43210, United States; Department of Mechanical and Aerospace Engineering, The Ohio State University, Columbus, Ohio 43210, United States; Department of Physics, The Ohio State University, Columbus, Ohio 43210, United States*

Author Contributions

E. M. M. synthesized, characterized, and analyzed the materials. L.D.T. aided in monomer synthesis. E.M.M. mounted and ran samples on the cryostat. B.W. assisted with the longitudinal, steady-state heat flow measurements and interpreting the data. J. P. H. and P. L. M. supervised the project. The manuscript was written by E.M. M. and P. L. M.

Notes

The authors declare no competing financial interests.

ACKNOWLEDGMENTS

We thank The Ohio State University (OSU) Campus Chemical Instrument Center (CCIC) and Tanya Whitmer for assistance with the ¹³C CP-MAS NMR measurements and access to the instrumentation. J. P. H. and B. L. W. acknowledges financial support from the National Science Foundation (CBET-2133718) and the Department of Defense (DoD) Science, Mathematics, and Research for Transformation (SMART) Scholarship Program.

REFERENCES

- (1) Côté, A. P.; Benin, A. I.; Ockwig, N. W.; O’Keeffe, M.; Matzger, A. J.; and Yaghi, O. M. Porous, Crystalline, Covalent Organic Frameworks. *Science* **2005**, *310*, 1166-1170.
- (2) Bisbey, R. P.; Dichtel, W. R. Covalent Organic Frameworks as a Platform for Multidimensional Polymerization. *ACS Central Science*, **2017**, *3*, 533-543.
- (3) Diercks, C. S.; Yaghi, O. M. The atom, the molecule, and the covalent organic framework. *Science* **2017**, *355*, aal1585.
- (4) Feng, X.; Ding, X.; Jiang, D. Covalent organic frameworks. *Chem Soc Rev*. **2012**, *41*, 6010-6022.
- (5) Haug, W. K.; Wolfson, E. R.; Morman, B. T.; Thomas, C. M.; McGrier, P. L. A Nickel-Doped Dehydrobenzoannulene-Based Two-Dimensional Covalent Organic Framework for the Reductive Cleavage of Inert Aryl C-S Bonds. *J. Am. Chem. Soc.* **2020**, *142*, 5521-5525.
- (6) Lin, S.; Diercks, C. S.; Zhang, Y.-B.; Kornienko, N.; Nichols, E. M.; Zhao, Y.; Paris, A. R.; Kim, D.; Yang, P.; Yaghi, O. M.; Chang, C. J. Covalent organic framework comprising cobalt porphyrins for catalytic CO₂ reduction in water. *Science*, **2015**, *349*, 1208-1213.
- (7) Chen, S.; Yuan, B.; Liu, G.; Zhang, D. Electrochemical Sensors Based on Covalent Organic Frameworks: A Critical Review. *Frontiers in Chemistry* **2020**, *8*, 601044.
- (8) Haug, W. K.; Moscarello, E. M.; Wolfson, E. R.; McGrier, P. L. The luminescent and photophysical properties of covalent organic frameworks. *Chem. Soc. Rev.* **2020**, *49*, 839-864.

- (9) Skorjanc, T.; Shetty, D.; Valant, M. Covalent Organic Polymers and Frameworks for Fluorescence-Based Sensors. *ACS Sens.* **2021**, *6*, 1461-1481.
- (10) Wolfson, E. R.; Schkeryantz, L.; Moscarello, E. M.; Fernandez, J. P.; Paszek, J.; Wu, Y.; Hadad, C. M.; McGrier, P. L. Alkynyl-Based Covalent Organic Frameworks as High-Performance Anode Materials for Potassium-Ion Batteries. *ACS Appl. Mater. Interfaces* **2021**, *13*, 41628-41636.
- (11) Wolfson, E. R.; Moscarello, E. M.; Haug, W. K.; McGrier, P. L. Covalent Organic Frameworks as Electrode Materials for Rechargeable Batteries. *Organic Materials* **2021**, *3*, 67-89.
- (12) Xu, F.; Yang, S.; Chen, X.; Liu, Q.; Li, H.; Wang, H.; Wei, B.; Jiang, D. Energy-storage covalent organic frameworks: improving performance via engineering polysulfide chains on walls. *Chem Sci*, **2019**, *10*, 6001-6006.
- (13) Furukawa, H.; Yaghi, O. M. Storage of Hydrogen, Methane, and Carbon Dioxide in Highly Porous Covalent Organic Frameworks for Clean Energy Applications. *J. Am. Chem. Soc.* **2009**, *131*, 8875-8883.
- (14) Rabbani, M. G.; Sekizkardes, A. K.; Kahveci, Z.; Reich, T. E.; Ding, R.; El-Kaderi, H. M. A 2D Mesoporous Imine-Linked Covalent Organic Framework for High Pressure Gas Storage Applications. *Chem. Eur. J.* **2013**, *19*, 3324-3328.
- (15) Vyas, V. S.; Vishwakarma, M.; Moudrakovski, I.; Haase, F.; Savasci, G.; Ochsenfeld, C.; Spatz, J. P.; Lotsch, B. V. Exploiting Non-covalent Interactions in an Imine-Based Covalent Organic Framework for Quercetin Delivery. *Adv. Mater.* **2016**, *28*, 8749-8754.
- (16) Bai, L.; Phua, S. Z. F.; Lim, W. Q.; Jana, A.; Luo, Z.; Tham, H. P.; Zhao, L.; Gao, Q.; Zhao, Y. Nanoscale covalent organic frameworks as smart carriers for drug delivery. *Chem. Commun.* **2016**, *52*, 4128-4131.
- (17) Xu, X. F.; Chen, J.; Zhou, J.; Li, B. W. Thermal Conductivity of Polymers and Their Nanocomposites. *Adv. Mater.* **2018**, *30*, 1705544.
- (18) Chen, J.; Ding, N.; Li, Z.; Wang, W. Organic polymer materials in the space environment. *Prog. Aerosp. Sci.* **2016**, *83*, 37-56.
- (19) Freitas, S. K. S.; Borges, R. S.; Merlini, C.; Barra, G. M. O.; Esteves, P. M. Thermal Conductivity of Covalent Organic Frameworks as a Function of Their Pore Size. *J. Phys. Chem. C.* **2017**, *121*, 27247-27252.
- (20) Babaei, H.; McGaughey, A. J. H.; Wilmer, C. E. Effect of pore size and shape on the thermal conductivity of metal-organic frameworks. *Chem. Sci.* **2017**, *8*, 583-589.
- (21) Evans, A. M.; Giri, A.; Sangwan, V. K.; Xun, S.; Bartnof, M.; Torres-Castanedo, C. G.; Balch, H. B.; Rahn, M. S.; Bradshaw, N. P.; Vitaku, E.; Burke, D. W.; Li, H.; Bedzyk, M. J.; Wang, F.; Bredas, J.-L.; Malen, J. A.; McGaughey, A. J. H.; Hersam, M. C.; Dichtel, W. R.; Hopkins, P. E. Thermally conductive ultra-low-k dielectric layers based on two-dimensional covalent organic frameworks. *Nat. Mater.* **2021**, *20*, 1142-1148.
- (22) Wang, X.; Ho, V.; Segalman, R. A.; Cahill, D. G. Thermal Conductivity of High-Modulus Polymer Fibers. *Macromolecules* **2013**, *46*, 4937-4943.
- (23) Pyles, D. A.; Crowe, J. W.; Baldwin, L. A.; McGrier, P. L. Synthesis of Benzobisoxazole-Linked Two-Dimensional Covalent Organic Frameworks and Their Carbon Dioxide Capture Properties. *ACS Macro. Lett.* **2016**, *5*, 1055-1058.
- (24) Pyles, D. A.; Coldren, W. H.; Eder, G. M.; Hadad, C. M.; McGrier, P. L.; Mechanistic investigations into the cyclization and crystallization of benzobisoxazole-linked two-dimensional covalent organic frameworks. *Chem. Sci.* **2018**, *9*, 6417-6423.
- (25) Xu, Y.; Wang, X.; Zhou, J.; Song, B.; Jiang, Z.; Lee, E. M. Y.; Huberman, S.; Gleason, K. K.; Chen, G. Molecular engineered conjugated polymer with high thermal conductivity. *Sci. Adv.* **2018**, *4*, eaar3031.
- (26) Scheling, P. K.; Phillpot, S. R.; Keblinski, P. Comparison of atomic-level simulation methods for computing thermal conductivity. *Phys. Rev. B.* **2002**, *65*, 144306.
- (27) Hu, L.; Evans, W. J.; Keblinski, P. One-dimensional phonon effects in direct molecular dynamics methods for thermal conductivity determination. *J. Appl. Phys.* **2011**, *110*, 113511.
- (28) Velde, G. T.; Bickelhaupt, F. M.; Baerends, E. J.; FonsecaGuerra, C.; Van Gisbergen, S. J. A.; Snijders, J. G.; Ziegler, T. Chemistry with ADF. *J. Comput. Chem.* **2001**, *22*, 931-967.
- (29) Park, M.; Lee, S.-C.; Kim, Y.-S. Length-dependent lattice thermal conductivity of graphene and its macroscopic limit. *J. Appl. Phys.* **2013**, *114*, 053506.
- (30) Dong, H.; Fan, Z.; Shi, L.; Harju, A.; Ala-Nissila, T. Equivalence of the equilibrium and the nonequilibrium molecular dynamics methods for thermal conductivity calculations: From bulk to nanowire silicon. *Phys. Rev. B.* **2018**, *97*, 094305.
- (31) Bannwarth, C.; Caldeweyher, E.; Ehlert, S.; Hansen, A.; Pracht, P.; Seibert, J.; Spicher, S.; Grimme, S. Extended tight-binding quantum chemistry methods. *WIREs Comput. Mol. Sci.* **2021**, *11*, e1493.
- (32) Rappe, A. K.; Casewit, C. J.; Colwell, K. S.; Goddard III, W. A.; Skiff, W. M. UFF, a full periodic table force field for molecular mechanics and molecular dynamics simulations. *J. Am. Chem. Soc.* **1992**, *114*, 10024-10035.
- (33) Hoover, W. G. Canonical dynamics: Equilibrium phase-space distributions. *Phys. Rev. A.* **1985**, *31*, 1695-1697.
- (34) Nose, S. A unified formulation of the constant temperature dynamics methods. *J. Chem. Phys.* **1984**, *81*, 511.
- (35) Martyna, G. J.; Klein, M. L.; Tuckerman, M. Nose-Hoover chains: The canonical ensemble via continuous dynamics. *J. Chem. Phys.* **1992**, *97*, 2635.
- (36) Liu, Y.; Feng, Y.; Huang, Z.; Zhang, X. Thermal Conductivity of 3D Boron-Based Covalent Organic Frameworks from Molecular Dynamics Simulations. *J. Phys. Chem. C.* **2016**, *120*, 17060-17068.
- (37) McGaughey, A. J. H.; Kaviani, M. Observation and description of phonon interactions in molecular dynamics simulations. *Phys. Rev. B.* **2005**, *71*, 184305.
- (38) Zhang, X.; Jiang, J. Thermal Conductivity of Zeolitic Imidazolate Framework-8: A Molecular Simulation Study. *J. Phys. Chem. C.* **2013**, *117*, 18441-18447.
- (39) Slack, Glen A. Thermal Conductivity of Nonmetallic Crystals. *Solid State Physics* **1979**, *34*, 1-71.
- (40) Feng, D.; Feng, H.; Liu, Y.; Zhang, W.; Yan, Y.; Zhang, X. Thermal Conductivity of a 2D Covalent Organic Framework and Its Enhancement Using Fullerene 3D Self-Assembly: a Molecular Dynamics Simulation. *J. Phys. Chem. C.* **2020**, *124*, 8386-8393.
- (41) Giri, A.; Hopkins, P. E. Heat Transfer Mechanisms and Tunable Thermal Conductivity Anisotropy in two-Dimensional Covalent Organic Frameworks with Adsorbed Gases. *Nano Lett.* **2021**, *21*, 6188-6193.
- (42) Liu, J.; McCullough, R. D. End Group Modification of Regio-regular Polythiophene through Postpolymerization Functionalization. *Macromolecules.* **2002**, *35*, 9882-9889.